# A multi-directional redundant 3D-LPT system for ship–flight–deck wind interactions

Hysa, Ilda; Tuinstra, Marthijn; Sciacchitano, Andrea; Scarano, Fulvio; van der Meulen, Mark-Jan; Rockstroh, Thomas; Roosenboom, Eric W.M.

**DOI**
10.1007/s00348-024-03867-0

**Publication date**
2024

**Document Version**
Final published version

**Published in**
Experiments in Fluids

Experiments in Fluids (2024) 65:126
https://doi.org/10.1007/s00348-024-03867-0

RESEARCH ARTICLE

# A multi-directional redundant 3D-LPT system for ship–flight–deck wind interactions

**Ilda Hysa[1,2] · Marthijn Tuinstra[1] · Andrea Sciacchitano[2] · Fulvio Scarano[2] · Mark-Jan van der Meulen[1] · Thomas Rockstroh[3] · Eric W. M. Roosenboom[4]**

Received: 15 January 2024 / Revised: 15 May 2024 / Accepted: 6 August 2024 / Published online: 17 August 2024


**Abstract**

In the past years, volumetric velocimetry measurements with helium-filled soap bubbles as tracer particles have been introduced in wind tunnel experiments and performed at large-scale, enabling the study of complex body aerodynamics. A limiting factor is identified in the field of wind engineering, where the flow around ships is frequently investigated. Considering multiple wind directions, the optical access for illumination and 3D imaging rapidly erodes the measurement regions due to shadows and incomplete triangulation. This work formalizes the concepts of volumetric losses and camera redundancy, and examines the performance of multi-directional illumination and imaging for monolithic and partitioned modes. The work is corroborated by experiments around a representative ship model. The study shows that a redundant system of cameras yields the largest measurement volume when partitioned into subsystems. The 3D measurements employing two illumination directions and seven cameras, yield the time-averaged velocity field around the ship. Regions of flow separation and recirculation are revealed, as well as sets of counter-rotating vortices in several stations from the ship bow to the flight–deck. The unsteady regime at the flight–deck is examined by proper orthogonal decomposition, indicating that the technique is suited for the analysis of large-scale unsteady flow features.

## 1 Introduction

Stereoscopic particle image velocimetry (PIV) is a widespread technique for the study of complex three-dimensional flows in industrial wind tunnels. However, in the recent years, developments from planar to volumetric PIV have evolved 3D measurements to a level of versatility and up to a scale that enables their application in industrial aerodynamics. In situ calibration and precise realignments (Wieneke 2008, 2013) have simplified the setup of 3D imaging systems. The introduction of the Lagrangian particle tracking (LPT) with the Shake-the-Box algorithm (Schanz et al. 2016) has accelerated the data processing by orders of magnitude, compared to the treatment by tomographic PIV (Elsinga et al. 2006). A missing part of the extrapolation to industrial scale has been contributed with the introduction of helium-filled soap bubbles (HFSB) as tracers in wind tunnel flows (Scarano et al. 2015), (Caridi 2018) and (Faleiros et al. 2019), enabling to cover volumetric domains in the order of the cubic meter, with the same illumination devices used for planar PIV. Examples of direct applications in aeronautics have been given in the work of Faleiros (2021) around a tilt–rotor aircraft.

Despite the above advancements, a frequently encountered bottleneck of 3D measurements is the limited spatial coverage around complex model geometries, arising from restrictions in the optical access.

A measurement volume in 3D particle imaging is achieved by ensuring that the entire region of interest is illuminated and imaged clearly without obstructions or distortions. This issue is not problematic in laboratory settings where simple geometries are studied, or where the object is kept out of view (e.g., wakes, jets and boundary layers); however, optical obstructions become limiting in some large-scale applications. For instance, in the recent

✉ Ilda Hysa
ilda.hysa@nlr.nl

1 Netherlands Aerospace Center NLR, 8016 PR Marknesse, The Netherlands

2 Delft University of Technology, 2629 HS Delft, The Netherlands

3 LaVision GmbH, Anna-Vandenhoeck-Ring 19, 37081 Goettingen, Germany

4 Damen Naval, PO Box 555, 4380 AN Vlissingen, The Netherlands

3D measurement around a jet aircraft model (Hysa et al. 2023), the domain of interest, around the thrust-reversers, contains several regions of blocked optical access because of the complex configuration, whereby either illumination is missing or the imaging is obstructed. The problem is further exacerbated in the field of wind engineering, where the aerodynamic interaction around groups of objects needs to be evaluated over a range of wind directions (often around 360 degrees).

A variety of techniques have been devised to overcome optical blockage in PIV. Challenging applications such as velocity measurements inside the geometrically complex model of a human carotid were carried out by Buchmann et al. (2011). Measurements in internal combustion engines (Fajardo and Sick 2009) and turbomachinery also pose specific problems related to optical access. In multi-phase flows, Poelma (2020) succeeded in the measurement of the flow across an opaque medium. Successful extensions to the standard optical techniques include the refractive index matching (Uzol et al. 2002) in liquid flows, the use of fluorescent tracers to reduce laser reflections (Häfeli et al. 2014) and optical coherence tomography (Poelma 2020). Despite their innovative character, these solutions mostly apply to liquid flows, whereas for air flows, alternatives remain limited.

In turbomachinery applications, single-view 3D PIV and PTV techniques have been based on plenoptic imaging (Fahringer et al. 2015). This technique operates with minimal optical access, at the expense of optical aperture and, in turn, the precision of particle depth positioning. This highlights the importance of multi-directional imaging as twofold: domain imaging coverage and accurate particle positioning by large-aperture systems. Attempts to improve the latter with a mirror system (multiple eye PIV) have been proposed by Maekawa & Sakakibara (2018), but its extrapolation to large-scale measurements has not been yet devised.

Other approaches which could effectively extend the measured volume are based on spatial scanning where the measurement volume is covered by non-simultaneous sessions. The work by (Hoyer et al. 2005) presents a 3D scanning PTV approach, albeit at small scale. For large-scale application, scanning stereo-PIV has been demonstrated around helicopter models by De Gregorio et al. (2012) and Raffel et al. (2017), and more recently by Faleiros (2021) using HFSB. In all these cases, however, obstructed views are omitted, which often limits the measurement domain to a fraction of the domain of interest.

The introduction of robotic volumetric PIV (Jux et al. 2018), based on the concept of coaxial 3D velocimetry (Schneiders et al. 2018), was demonstrated with the measurements around the complex geometry of a full-scale cyclist model. Furthermore, its application at the German–Dutch WIND TUNNELs (DNW) returned the time-average velocity field around a scaled turbo-prop aircraft model (Sciacchitano et al. 2018). The robotic manipulation effectively circumvents the optically obstructing elements and allows a rapid positioning of the axial velocimeter. Among the shortcomings of this technique are the lower accuracy along the viewing direction (similar to that of plenoptic systems), the potential aerodynamic interference of the robotic system and the flow field and the increased measurement time due to scanning. Furthermore, unsteady fluctuations are typically not captured by this approach.

Extending the above optical access techniques to the context of wind engineering, to additionally include the investigation of the unsteady aerodynamic effects, has not been afforded so far. In particular, the study of the unsteady flow behavior above the ship–flight–deck presents a challenge, where the fluctuating wind conditions can adversely affect the launch and recovery of aircraft and UAV from the flight–deck, particularly rotorcraft (Zan 2005).

The specific aerodynamic investigation of the flow around a ship has been covered with a number of studies aiming at characterizing the complex and turbulent environment caused by the wind–ship interaction. Previous experimental research on ship aerodynamics and the nature of the airwake has made use of typically pointwise measurement techniques: multi-hole pressure probes (Miklosovic et al. 2011); hot-wire anemometry (Healey, 2012) and laser Doppler velocimetry. Qualitative inspection of the flow was done with smoke flow visualization (Kulkarni et al. 2005). Planar PIV was employed to yield more details about the spatial organization of the flow (Rosenfeld et al. 2015; Seth et al. 2021), and recently, a dual-plane PIV experiment (Zhu et al. 2024) has yielded an increased level of detail in the organization of large-scale turbulent structures. A first study employing tomographic PTV (Vidales et al. 2016) was restricted to the rear deck, where the proper orthogonal decomposition method was used to understand the global structure of the unsteady velocity fluctuations.

More comprehensive investigations of this problem are conducted with CFD techniques, which require extensive validation in view of the number of parameters involved (ship geometry, wind direction, atmospheric boundary layer and coherence of flow fluctuations). Therefore, solutions are sought that enable comprehensive measurements for comparison and verification.

The present work examines the use of a redundant illumination and imaging system to extend the spatial coverage of 3D-LPT measurements to include the study of the unsteady aerodynamic effects. For this purpose, two-directional illumination and seven-directional imaging have been deployed for the case study of the wind aerodynamics around a representative ship model.

The article first introduces the problem of optical blockage, as the basis of the measurement volume reduction. In

the first section, the relevant parameters governing the problem of illumination and imaging with a redundant system are introduced. Furthermore, the possible system configurations are presented and discussed in terms of the expected measurement performance. The following section describes the experimental apparatus, its configuration and the measurement procedure. The fourth section presents and discusses the results in terms of global flow field topology, with a specific discussion about the behavior at the flight–deck where most literature is focused.

## 2 Three-dimensional imaging and volumetric illumination

This section introduces the definitions and operations necessary to study the problem of optical blockage for LPT measurements. The geometry used for this assessment is the same as that of the model that was tested in the wind tunnel, and it is shown in Fig. 1. Although the concepts are illustrated using the specific example of the ship geometry at several angles, the analysis reported below, in particular the equations that describe the volume losses remain of general validity, and it can be applied to a variety of experiments where a redundant illumination and imaging system is used around a complex geometry.

The following variables are defined: $S_i$ denotes the shadow volume resulting from the *i*th illumination source, and $V_{tot,S}$ denotes the total shadow region, resulting from a combination of different illuminations. For the imaging, $C_i$ denotes the occlusion region (volume) where the optical access of camera *i* is blocked, with $V_{tot,C}$ being the total occluded region. The tomographic aperture between sets of cameras *i* and *j* is measured by $\beta_{i,j}$. Measurements are performed around the domain of interest (DOI). If a fraction of the domain is not measured, that is considered an imaging loss and is represented by the variable $V_{\text{loss}}$.

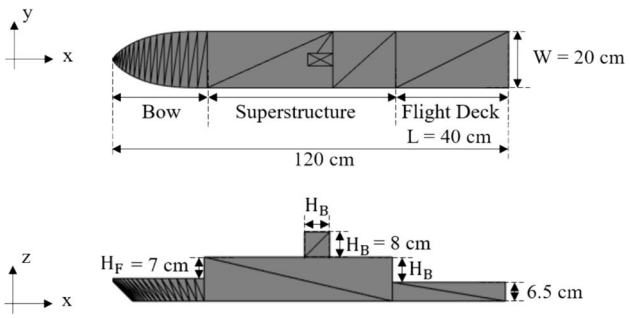


**Fig. 1** Schematic geometry (at scale) of the ship model along with main dimensions and part nomenclature

In order to quantify the losses in a systematic way, simple elements of set theory are used. These are presented schematically in Fig. 2. The largest set is the DOI, plotted here as the outlining rectangle. Inside the DOI, subsets are denoted as circles, named here A and B. These subsets that represent the losses regions can be combined using the operations of intersection-∩-or union-∪-, depending on the logics of the case.

In general, minimizing the intersection between two sets translates to minimizing the number of common elements between them. For the union, the opposite is true, minimizing the union is achieved by maximizing the number of common elements between the sets.

### 2.1 Constrained illumination

The problem of optical blockage due to shadow forming is simple in principle, by treating shadows with ray tracing of geometrical optics, under the assumption of parallel illumination. However, the problem complexity arises when a multitude of illumination directions are considered in three-dimensional space, where the illuminated object also undergoes rotation. Redundant illumination is an effective approach to reduce the measurement volume erosion: A region in shadowed from a given direction can be illuminated from a second or a third one. On Fig. 3-top, the shadows around the model are shown for the case of a single illumination, along with the DOI (green rectangle) in the first condition. The rotation of the model is denoted by the yaw angle $\gamma$, and the elevation of the illumination source with respect to the center of the DOI is denoted by the elevation angle $\alpha$. Shadows are formed at different locations for every orientation of the object. A measurement point is considered valid when data are obtained at all angular positions. The consequence of the latter for the single illumination direction is that almost no point in the domain is imaged at all the rotation steps. The second row illustrates the improved situation by adding a second, orthogonal, illumination direction. The overall losses drop from 75% (additive) with one illumination direction, to 41% with a second illumination.

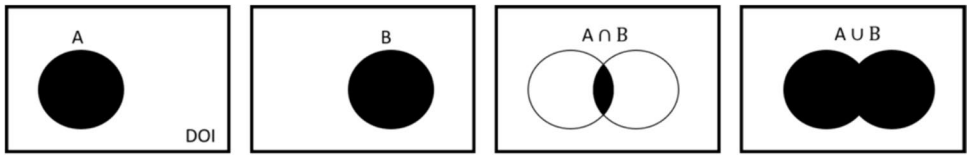


**Fig. 2** Schematic of the elements of set theory used in the volume losses quantification

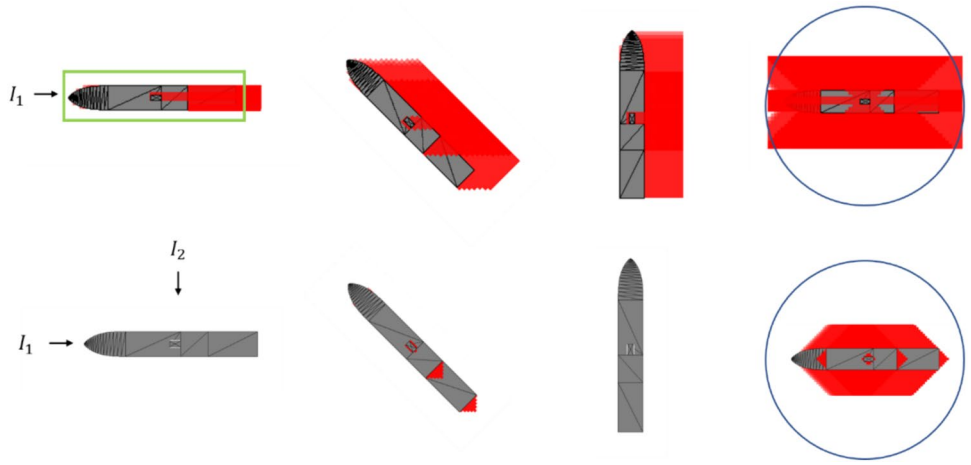


**Fig. 3** Top view of the shadows (in red) resulting from single (top) and double (bottom) illumination directions. The model is rotated counter-clockwise in steps of $\gamma = 45°$ (from left to right) as to represent different wind conditions. Last image on the right illustrates the cumulative effect over 360° rotation at illumination elevation $\alpha = 0°$

**Table 1** Summary of volume losses for a full rotation of the model, with varying number of illumination directions and elevation angle

| Illumination elevation angle (α) | | $V_{tot,S}$ (%) | |
|---|---|---|---|
| 0° | Yaw angle ($\gamma$) | #1 | #2 |
| | 0° | 9 | 0.2s |
| | 45° | 16 | 2 |
| | 90° | 14 | 0.2 |
| | (0:45:360)° | 75 | 41 |
| 30° | 0° | 2 | 0.2 |
| | 45° | 11 | 1 |
| | 90° | 10 | 0.2 |
| | (0:45:360)° | 48 | 35 |
| 60° | 0° | 1 | 0.2 |
| | 45° | 6 | 0.5 |
| | 90° | 6 | 0.2 |
| | (0:45:360)° | 33 | 27 |

Considering a system illuminated from $M$ directions, the expression of the volumetric losses due to shadows reads as follows:

$$V_{tot,S} = S_1 \cap S_2 \cap \ldots \cap S_M \tag{1}$$

based on the fact that a region in shadow from a given direction can be illuminated from an $M$th direction, the total shadowed region is gradually eliminated with the addition of illumination directions.

Figure 3 illustrates the limiting case of the illuminators being at 0° elevation angle. When the elevation angle is increased, the shadowed volume decreases, as this particular model has a convex geometry. The results from the ray tracing analysis around this model at three different elevation angles are summarized in Table 1. Adding a second illumination direction and increasing the elevation angle from 0 to 60° result in a rapid decrease in the overall volume losses from 75 to 27% of the DOI.

## 2.2 Imaging in the presence of obstructions

In the present section, the concept of optical access to a complex object from several directions is discussed with the purpose of explaining different approaches and options to imaging. As discussed in the literature, systems for 3D particle tracking typically comprise 3–4 cameras, which subtend a solid angle such to accurately triangulate the position of the illuminated particle tracers in physical space. In the present discussion, the algorithm Shake-the-Box (STB), used for LPT, is considered as a baseline for the analysis of the images set (Schanz et al. 2016). Although a number of methods and variants of particle tracking exist and have been proposed in the literature (most notably, Maas et al. 1993, among others), STB is a prominent technique, which has been rapidly adopted in the experimental fluid mechanics community (Schröder and Schanz 2023). The use of 3–4 cameras is typically reported as sufficient to accurately describe particle distributions resulting in an image seeding density in the order of $10^{-2}$ to $10^{-1}$ particles per pixel (ppp). The losses that would result from a standard three camera volumetric system are illustrated in Fig. 4, for three rotation angles that correspond to those considered for the illumination in the previous section, as well as the total. For the sake of clarity, only a plane at the ship mid-height is plotted, under the simplification of parallel imaging.

Flow measurements can only be performed within regions in view by all the cameras; hence, the total losses due to optical blockage are in fact equal to the combination, i.e., union of all the individual camera losses (as opposed to the intersection in the case of illumination) expressed in Eq. (2).

$$V_{tot,C} = C_1 \cup C_2 \cup C_3 \tag{2}$$

Since the losses are combined, a minimal geometrical loss scenario is achieved when the individual losses intersect maximally, i.e., when the cameras are placed as close

to each other as possible, coaxial imaging ($\beta_{i,j} \rightarrow 0$). However, this is detrimental for the reconstruction accuracy (Scarano 2013).

In all tomographic imaging systems where the total number of cameras is equal to the number of cameras needed for reconstruction, there is a conflict between minimizing losses and maximizing reconstruction accuracy, as $\beta_{i,j}$ increases → $V_{\text{loss}}$ increases.

The total measurement volume that is not accessible to measurements is a result of either a shadow from the illumination or the cameras' blocked line of sight and can be defined as follows:

$$V_{loss} = \text{DOI} \cap \left(V_{tot,S} \cup V_{tot,C}\right) \tag{3}$$

An overview of the total losses for a system comprising three cameras and a single illuminator is given in Table 2. It should be remarked that these values are problem dependent, and as such, they only give an impression of the typical losses, rather than to provide exact figures. The actual value of the volume loss is strongly dependent on parameters such as object shape and connectivity, cameras and laser positioning. Additionally, the same situation that was presented previously for the elevation angle of the illumination is valid here for the cameras. It is clear that in the present case, the losses for the full rotation of the model completely hamper the measurements, while at each position, they may still be considered as acceptable. This motivates the analysis of redundant imaging systems, where more imaging directions are necessary in order to extend the measured volume, which is presented in the following section.

**Table 2** Losses for a three camera, one illumination 3D-LPT system

| Model yaw angle (°) | $V_{\text{tot},C}(\%)$ | $V_{\text{tot},S}(\%)$ | $V_{\text{loss}}(\%)$ |
|---|---|---|---|
| 0 | 21 | 9 | 23 |
| 45 | 24 | 16 | 32 |
| 90 | 41 | 14 | 51 |
| (0:45:360) | 100 | 75 | 100 |

### 2.2.1 Redundant imaging

In the present context, a 3D particle imaging system is denoted as redundant when the number of cameras (viz. views) largely exceeds the above minimum of three.

A redundant system can be operated in two different modes, depending on the logics imposed for the detection of a particle. In the monolithic mode, a particle tracer is detected if its image is found on each image of the set. Conversely, a partitioned system splits the camera set into independent subsets. Each subset operates separately to detect particle images. A consequence of the monolithic approach is that when a tracer is not in view from one of the cameras (e.g., if the view is blocked by the presence of a solid object), the particle is not detected. The same rule applies to a partitioned system, but to each subset separately.

A monolithic system, therefore, can potentially reconstruct particle fields at high concentration with minimal occurrence of ghost particles (Elsinga et al. 2011). However, for such system, particle detection may be hampered by the weakest link, i.e., the particle detection may fail based on a single view being obstructed by the object.

Conversely, the partitioned system is more prone to the occurrence of ghost particles. The main advantage of such system is that a particle not in view by one of the cameras in a given subset may be in view from all the other cameras of another subset. In this respect, the system is more resilient to optical obstructions.

The above concepts are depicted schematically in Fig. 5, where the situation is exemplified with three particles in the surrounding of the model. Particle A is in view of 5 cameras, particle B in view of 4, and particle C in view of 3. What regions of the domain, and which particles will be detected, depends on how the system is operated, more specifically on how many cameras are requested for the reconstruction.

The result of a monolithic system where all cameras are required is that none of the points will be detected. The reconstructed regions for different numbers of activated cameras are plotted in Fig. 5 in green, for the same plane as in Fig. 4.

An expression can be derived that describes $V_{\text{loss,I}}$ for a monolithic system, and it is presented below. The expression is given for a system comprising $N$ cameras.

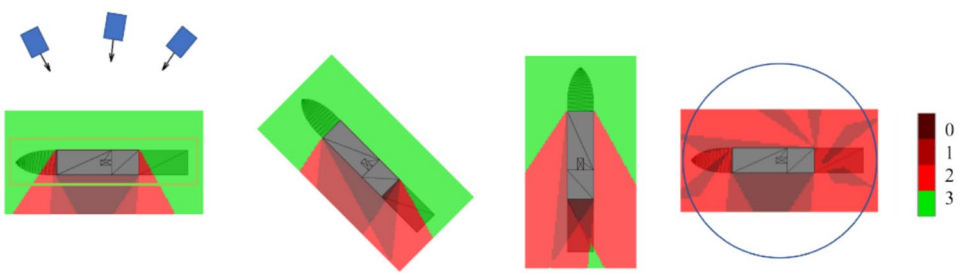


**Fig. 4** Three-dimensional imaging around the ship model at rotation of 0, 45, 90° and full rotation additive (left to right) plotted on a plane at the mid-deck height. The different colors represent the number of cameras with clear optical access at any given region

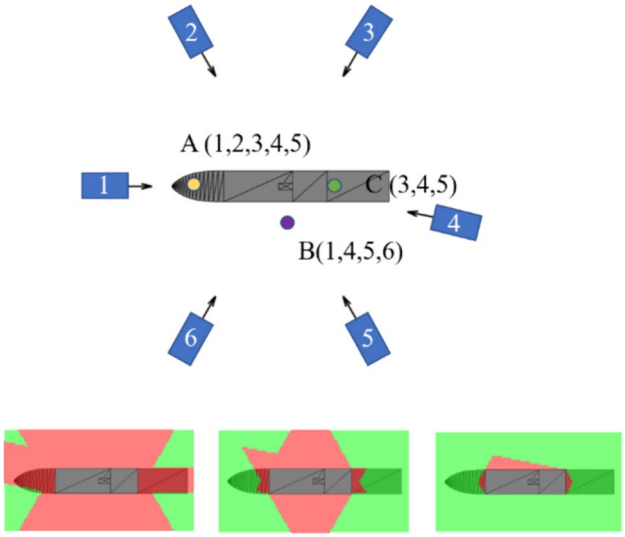


**Fig. 5** Losses (in red) resulting from a redundant camera system depending on the mode it is operated. Bottom row: (Left) Monolithic system, all six cameras are required for the reconstruction, (Middle) partitioned system with groups of 5 and (Right) partitioned system with groups of 4

$$V_{loss,C} = C_1 \cup C_2 \cup \ldots \cup C_N \tag{4}$$

The same quantity for a system partitioned into subset of three cameras reads as follows:

$$V_{loss,C} = (C_1 \cup C_2 \cup C_3) \cap (C_1 \cup C_3 \cup C_4) \cap \ldots \cap (C_4 \cup C_5 \cup C_6) \tag{5}$$

The number of camera subsystems available for reconstruction is the number of combinations of $N_{min}$, the minimum number of cameras required to reconstructed 3D positions, out of $N$, the total number of cameras available and reads as follows:

$$N_{sub} = \frac{N!}{N_{min}!(N - N_{min})!} \tag{6}$$

The losses associated to each operating mode are summarized in Fig. 6 and expanded for the consideration of the cameras' elevation angles 0, 30 and 60° (in accordance with the results shown for the illumination). It can be clearly seen that requiring fewer cameras for particle triangulation, greatly increases the number of camera subsystems available from 1 when all 6 cameras are required, to 20 when a minimum of 3 is required. This results in a dramatic gain of approx. 60% of the DOI. It should be retained in mind, however, that the reducing the number of cameras of a subset will make the system prone to generating ghost particles.

Finally, as the elevation angle is increased, the losses decrease, as expected from the analogous results from the illumination.

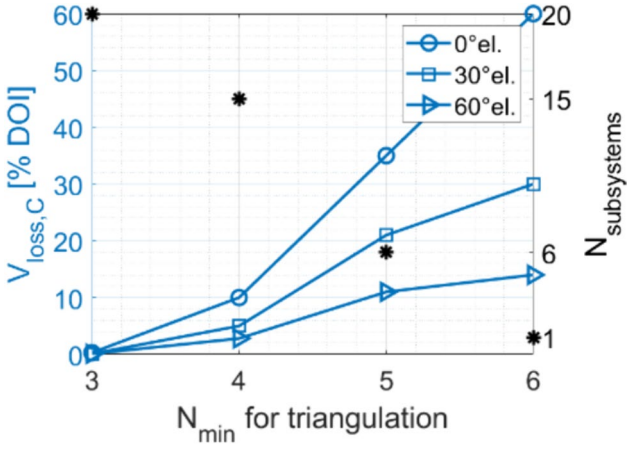


**Fig. 6** Plot of the imaging losses and number of available camera subsystems resulting from different operating modes of the redundant camera system

One result of Eq. (5) is that when redundant cameras are available, and the system is operated in a partitioned mode, a larger overall measurement region can be achieved by placing the cameras such that their occluded regions intersect minimally. This corresponds to the condition whereby the cameras' placement maximizes $\beta_{i,j}$ for every subset. As a result, the system does not suffer from the conflict of $V_{loss}$ and $\beta$ described for monolithic LPT systems. Furthermore, this condition offers increased freedom in the placement of the cameras and potential to optimize the imaging system for both minimal losses and optimal reconstruction quality.

Based on Eqs. 1–6, a loss parameter is defined to quantify the performance in terms of volumetric coverage, of a multi-directional system.

A criterion based on the condition that the volumetric measurement loss does not exceed 5% of the domain of interest is introduced, namely:

$$V_{loss} = DOI \cap \left(V_{tot,S} \cup V_{tot,C}\right) < 5\%\ \mathrm{DOI} \tag{7}$$

Although arbitrary, this value suggests that multi-directional redundant camera systems should be designed to meet this criterion, when the losses due to optical obstruction are to be neglected.

In Fig. 6, the losses associated to the partitioned mode of operation of the redundant camera systems can be contained to 0.3% of the DOI, in contrast with those resulting from a single system comprising three cameras, as shown in Table 2. Even considering only the case of a single position (at 0 degrees yaw), which will be the subject of the following sections, the redundant imaging reduces the amount of volume losses dramatically, from the initial value of 20%. This allows to satisfy the loss criterion and highlights the necessity for multi-directional imaging. The concepts given

above are put into practice and illustrated with an experimental realization of a multi-directional redundant 3D-LPT measurement.

## 3 Experiments around a ship model

### 3.1 Experimental apparatus

Experiments were performed in the aero-acoustic wind tunnel AWT of the Netherlands Aerospace Center (NLR). The AWT is a closed section wind tunnel with $80 \times 60$ cm$^2$ cross-section, operated at a free-stream velocity of 10 m/s. AWT is configured as an open jet for the present experiment, to maximize optical access. The ship model was a simplified frigate type of 1:60 scale (Van Muijden et al. 2013) mounted on a flat plate, reproducing the see surface. The model was installed upside down to simplify the placement of the cameras and illumination from the ground. The Reynolds number ($Re_H = 60{,}000$) is based on the height of the ship superstructure ($H_B = 8$ cm). A typical full scale Reynolds number is in the order of $10^8$. Although in general, Reynolds equality is required for the wind tunnel scaling, bluff bodies with sharp angular features such as the superstructure of the ship exhibit only a weak dependence with Reynolds as long as the separated region remains in the turbulent regime. For reference, a minimum Re of $11 \times 10^3$ is proposed by Healey (1992) and widely accepted for ship airwake modeling. Wall et al. (2022) have also argued that increasing Re above this value the flow behavior is invariant over a wide range of Reynolds numbers. Therefore, it is argued that the effects are representative of the full scale.

Neutrally buoyant HFSB with 0.45 mm mean diameter were employed as flow tracers. An in-house developed seeding rake comprising 56 generators is installed in the settling chamber of the AWT. The pitch between generators is 15 cm in either direction. The system delivers approx. $1.4 \times 10^6$ tracers per second. The seeding generator unit was controlled through an in-house built fluid supply unit. At a free-stream velocity of 10 m/s, the seeding concentration of the undisturbed flow is estimated as approx. 1.1 tracers/cm$^3$, (varying from 1 to 2 tracers/cm$^3$ across the measurement domain) resulting in a particle per pixel value of approx. 0.01.

The particles were illuminated with a Quantel Evergreen Nd:YAG ($2 \times 300$ mJ/pulse, $\lambda = 532$ nm). Bi-directional illumination was achieved by sending the laser beam through a beam splitter, which greatly reduces the regions of total shadow in the domain of interest. The two split beams were then expanded with $f = -100$ mm spherical lenses and diffused through diffuser grids to achieve a more homogeneous illumination intensity. This setup resulted in the illumination of the domain from two directions as depicted with green arrows in Fig. 7.

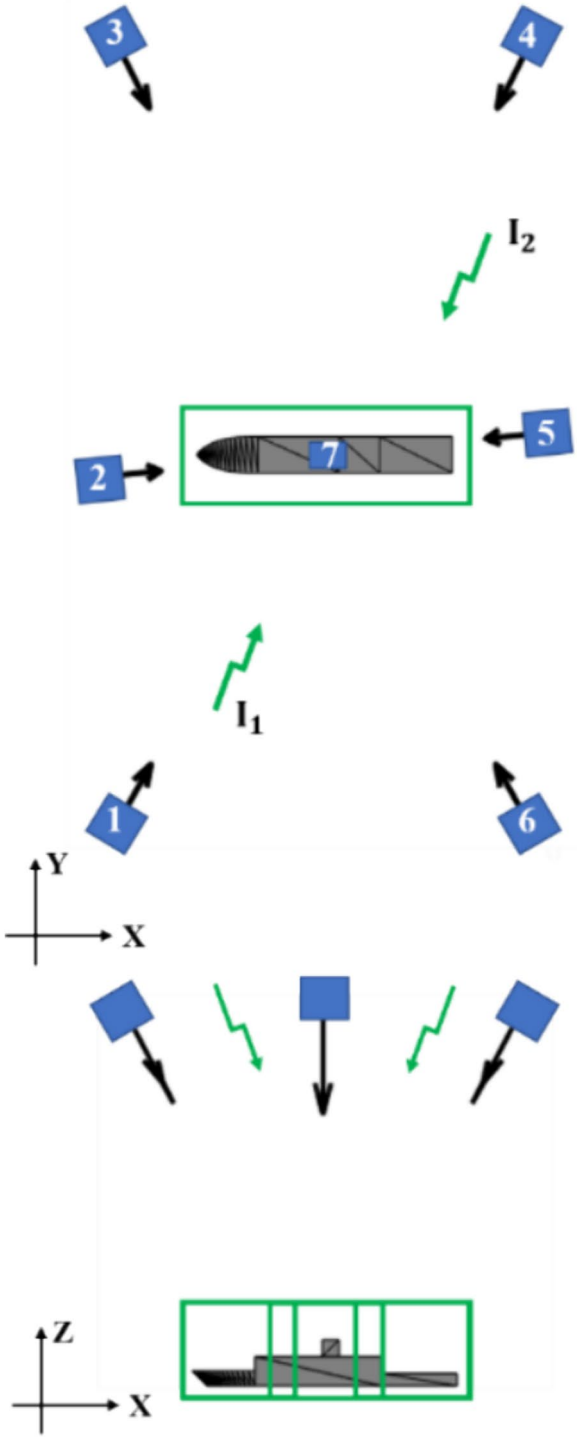


**Fig. 7** Sketch of the 3D-LPT setup (distances not to scale)

#### 3.1.1 Imaging and recording

The 3D imaging system comprised seven LaVision Imager *LX* CCD cameras (1620×1220 pixels, 4.4 µm pixel pitch, 10 bits), equipped with $f = 35$ mm objectives, set at a numerical aperture $f\# = 8$. The latter yielded sufficient depth of field to obtain sharp particle images along a depth of 40 cm. To achieve a compromise between the field of view (FoV) and spatial resolution, given the dimensions of the model (120 cm length to 40 cm width), the domain was analyzed in three separate sections, covered by translating the model and separated by 50 cm. This was achieved without rearrangement of illumination and imaging systems. A schematic view of the cameras' positions and viewing directions is shown in Fig. 7.

The largest tomographic angle in the setup is 85°, and the smallest in a subsystem is 40°. The elevation of the cameras under these imaging conditions is approx. 45°. At the chosen free-stream velocity, a time separation of $\Delta t = 350$ µs yields a maximum particle image displacement of approx. 10 pixels. Measurements sequences are acquired at a rate of 7.55 Hz, with 230 recordings for each segment. Table 3 summarizes the measurement parameters.

System calibration is crucial for the accurate reconstruction of particle positions. Several advancements have been recent proposed in the field of calibration from multiple cameras for large-scale experiments. One such study is that by Muller et al. (2020), where calibration was done using a freely moving calibration target. However, in the present study, to minimize the complexity of the setup, the imaging system calibration yielding the world-to-image mapping function was performed with a standard PIV calibration plate, translated along the depth, prior to model installation. The geometric calibration was followed by a correction procedure (volume self-calibration, Wieneke 2008) reducing residual reprojection errors to a fraction of a pixel. Synchronization of illumination and image acquisition and data recording and display were achieved with a LaVision programmable timing unit (*PTU-X*) and controlled with *DaVis* 8 software.

**Table 3** Volumetric measurement parameters

| Parameter | Value |
|---|---|
| Laser pulse separation (double-pulse) [µs] | 350 |
| Recording frequency [Hz] | 7.55 |
| Sensor size [pixels] | 1620×1220 |
| Image sensor pixel pitch [µm] | 4.4 |
| Magnification | 0.0126 |
| Objective focal length [mm] | 35 |
| Numerical aperture *f*# | 8 |
| Measurement domain | 0.6×0.5×0.4 $m^3$ |
| Nr. of recordings | 230 |

#### 3.1.2 Particle reconstruction

Data processing was done in *DaVis* 10, using the Shake-The-Box (STB) algorithm (Schanz et al. 2016) adapted for double-frame recordings, in a research version of the software. Within STB, specific modifications for the processing of data acquired with a system of redundant cameras are only necessary in the iterative particle reconstruction part (IPR) procedure (Wieneke 2013; Jahn et al. 2021), where the algorithm needs to be adapted to allow for sub-groups of cameras to contribute to the reconstruction. Within IPR, particles were added in four iterations (of the outer and inner loops of the algorithm), within an allowed triangulation error of 0.5 px. A minimum of three cameras was specified as a lower limit for particle reconstruction. The number of detected tracks (paired particles) obtained from the monolithic approach is approximately 20% that returned by the partitioned method (approx. 15,000), as shown in Fig. 8. The ratio of 20% for the monolithic approach is consistent with the analysis performed in Sect. 2. For completeness, the results from some subsystems of three or four cameras are shown. Clearly, the choice of the observation direction largely impacts the volume losses and, in turn, the amount of detected tracks. A minimum of only 700 tracks are tracked with the subsystems 2–5–7, due to the limited field of view of camera 7 (placed directly above the model). In general, systems of three or four cameras yield 1000–3000 tracks, which is a visibly smaller amount compared with the redundant, partitioned imaging system.

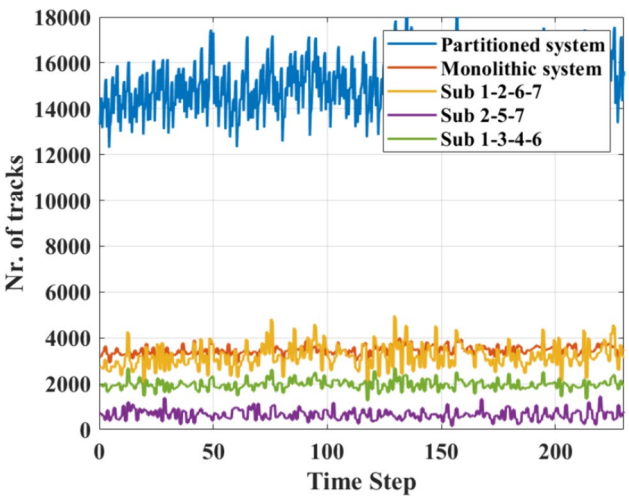


**Fig. 8** Number of particles tracked with different approaches/camera sub-groups

#### 3.1.3 Velocity evaluation

The instantaneous velocity of each particle tracer is evaluated at the midpoint of the particle pair, at scattered locations. The time-average velocity is brought into a Cartesian grid by ensemble averaging the velocity of particle tracers belonging over cubic cells of $2 \times 2 \times 2$ cm$^3$. Given the spatial concentration and the number of recordings, each bin collects approximately 2500–5000 samples. Furthermore, the velocity vectors are spaced by 0.5 cm as a result of 75% overlap among neighboring bins. Each separate measurement domain encompasses $60 \times 50 \times 40$ cm$^3$, and the velocity field is described with a grid of $158 \times 131 \times 105$ nodes. The composite measurement covers a domain of $130 \times 50 \times 40$ cm$^3$ with $260 \times 151 \times 80$ nodes. At the edges of the DOI, the concentration of detected tracers decays and with it the number of samples comprised in a single bin. The validity criterion for a velocity vector from a given bin is set to a minimum of 50 samples. Model translation resulted in small non-overlapping regions, visible as data gaps in the velocity fields presented in Sect. 4.1. This is due to the pyramidal shape of the FoV from each camera, unlike the assumption of parallel viewing rays taken for simplicity in the imaging analysis.

The main sources of velocity uncertainty estimation are identified as system calibration, particle triangulation and detection uncertainties, signal-to-noise (SNR) ratio of the particle images and errors in particle matching and tracking.

Regarding the calibration and particle detection uncertainties, after performing volume self-calibration (Wieneke 2008) on the particle images, the geometric calibration in this measurement was corrected to below 0.05 pixel accuracy. Additionally, given the relatively low ppp value of 0.01 and the tomographic aperture of most camera subsystems exceeding 45°, the ambiguities in particle detection and triangulation are minimal with the IPR algorithm (Scarano 2013; Wieneke 2013). The SNR of the pre-processed images is approx. 500, averaged across the domain, with the illumination intensity being approximately constant across the domain, spatially and temporally, and with minimal reflections due to the matte black painted model. Errors in matching and tracking are known to be higher for double-pulse measurements as compared to multi-pulse or time-resolved measurements where particles can be followed over several frames. A convergence analysis on the time-averaged results (omitted here for the sake of brevity) shows that the value of the mean velocity (for each component) converges within 2% (1%) of the free-stream value including 60 (180) measurements.

The maximum measured velocity is ~ 11 m/s. For the minimum resolvable velocity, an estimation of the local velocity uncertainty is determined by amplitude of velocity fluctuations u' divided by the square root of amount of particles $N_p$ in a bin. The latter estimator is averaged across the measurement domain, yielding a value of approx. 0.05 m/s, which corresponds to approx. 0.5% of the maximum measured velocity. A further discussion on the variation of the velocity fluctuations across the domain, particularly over the ship–flight–deck, is provided in Sect. 4.2.

The flow topology is illustrated displaying the time-averaged velocity field (velocity component iso-surfaces and cross-sections). Furthermore, when relevant, vorticity and Q-criterion are employed to describe the topology of vortices. The data are overlaid onto the CAD geometry of the ship model.

## 4 Results

### 4.1 Time-averaged flow topology

The airwake over the ship front side exhibits flow structures characteristic of flows over delta wings (bow segment), forward facing step (FFS) in the superstructure (Graziani et al. 2018; Largeau & Moriniere 2006; Barbosa-Saldaña & Anand 2007), surface-mounted prisms (the funnel) (Schröder et al. 2020; Sousa 2002) and backward facing step (BFS) at the rear deck (Chun & Sung 1998; Scarano et al. 1999; Spazzini et al. 2001; Piirto et al. 2003; Sung et al. 2004; Chovet et al. 2017). Many of the mentioned studies pertain to a Reynolds number in the order of $10^3$ and on a simplified 2D FFS or BFS geometry; nevertheless, some topological similarities are discussed.

Figure 9 shows a top and side view of the combined measurements over the entire ship, where time-averaged streamwise velocity contours are plotted in two planes: immediately above the superstructure ($z = 0.145$ m) and along the symmetry line ($y = 0$). Flow separation and recirculation is

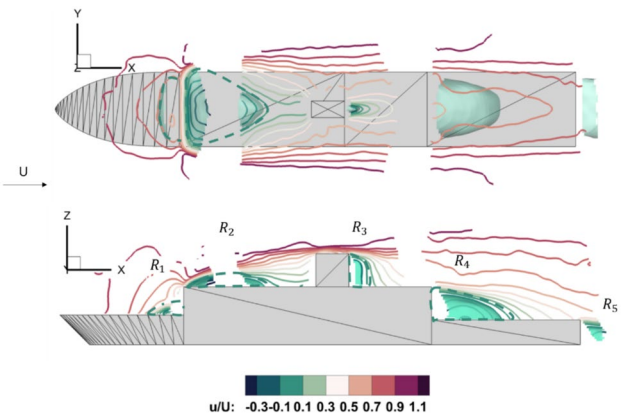


**Fig. 9** Time-averaged streamwise velocity contours on a horizontal plane at $z = 0.145$ m (top) and on the symmetry plane $y = 0$ (bottom) along with iso-surfaces of zero streamwise velocity. Dashed lines added around the recirculation regions, partially padding the data gaps

observed in five regions as reported in Fig. 9: $R_1$ denotes the recirculation due to the FFS imposed by the superstructure; given the sharp edge of the latter, the flow separates again when surpassing the front edge of the superstructure, resulting in $R_2$.

The flow separation in front of the prismatic funnel is not captured in the present experiments, likely due to the small size of its cross-section and the limited spatial resolution. Instead, the separated wake past it is clearly visible as $R_3$. Finally, the BFS imposed by the lower flight–deck produces a relatively large, separated region $R_4$ that will be scrutinized further with details of the fluctuating flow field. A last region of separation is observed trailing the fight–deck due to the downstream sharp edge of the deck. For better visibility, these recirculation regions are encompassed by the zero streamwise velocity iso-surfaces in the plot.

For the flow over the FFS, compared to studies of FFS flow in a 2D configuration, the three-dimensional effects (aspect ratio of the step $W/H_f = 2.8$) cause a pronounced difference. First, the finite span of the structure allows the flow to escape from the sides, which mitigates the strength of the adverse pressure gradient and delays the position of separation. The extent of the recirculation bubble at the foot is 0.8 $H_f$ (as defined in Fig. 1). Atop the superstructure front edge flow separates as the result of the sharp-edged structure. The reverse flow region extends downstream for a distance 2.8 $H_f$.

Further flow separation is encountered downstream over the funnel and above the flight–deck hangar, where the separated flow develops into 3D shear layers which enclose the regions of flow recirculation $R_3$ and $R_4$. From the velocity contours in the $z$-plane, it can be seen that the presence of the funnel creates a velocity deficit that extend downstream over the deck region.

The flow past the hangar over the flight–deck can be compared to 2D BFS along the model plane of symmetry; however, the 3D spanwise effects (AR = 2.5) are significant. The separated shear layer curves downward toward the reattachment zone and impinges on the deck wall. The distance from the vertical step wall to the impinging point is known as the reattachment length. Eaton and Johnston (1981) have reported that depending upon the upstream conditions, such as boundary layer state and thickness, free-stream turbulence, 2D BFS flows exhibit a reattachment length varying from four to eight step heights. In the present experiment, the turbulent incoming boundary layer combined with the aspect ratio of the geometry profoundly alters the dynamics of the flow yielding a relatively short separation, observed at approximately $2.5H_B$ and with the reattachment line featuring a straight segment in the middle plane and tapered toward the side edges. This behavior is consistent with the separation length and behavior past obstacles and prisms of limited span (Sung et al. 2004). The turbulent high-momentum flow at the sides of the separation entrains low-momentum fluid and such process justifies the quasi-linear tapered shape of the BFS separation region. The recirculation behind the step, which features low static pressure, is enclosed by the separated free shear layer, and this low-pressure region causes an inboard bending of the streamlines toward the mid-plane of symmetry of the deck. The recirculation zones are noted to be fairly symmetric in the time-averaged sense.

Further the streamwise vorticity distribution (Fig. 10) indicates the salient aspects of coherent vortices developing along the ship. Two counter-rotating vortices are formed along the edges over the bow, which induce a local separation and a pronounced downwash at the symmetry plane. This vortex system is more evident by iso-surfaces of streamwise vorticity plane in region a of Fig. 10. The vorticity is normalized with the free-stream velocity and the flight–deck step length, $\omega_x^* = {\omega_x}/{UH_B}$. The presence of this vortex system has been previously hypothesized by Tinney & Ukeiley (2009), interpreting the surface pattern of oil flow. Based on these traces along the outer edges of the bow segment of the ship, they concluded that it correspondeds to the formation and development of wing vortices, which is confirmed by this measurement.

Flow separation and reattachment introduce a high level of turbulent fluctuations upstream of the funnel and deck. The flow development around this structure exhibits some of the typical features reported for surface-mounted prisms, such as horseshoe vortex, tip separation and arc vortex at the back, (Schröder et al. 2020), which have been schematically sketched and plotted in Fig. 11.

The flow around the funnel results in a horseshoe vortex extending over the top of the superstructure and well downstream over the deck. Additionally, in the regions where separation over the side edges of the step is expected (section d, from Fig. 10), the formation of edge vortices is observed, as also clarified in Fig. 11, due to the spanwise entrainment of fluid from below the surface of the step. These findings regarding the flow topology are in agreement with the deduced flow topology in the works of Tinney & Ukeiley (2009) and Vidales (2016).

Supplementary digital material is provided in form animations to aid the detailed visualization of the flow structure.

### 4.2 Unsteady behavior on the flight–deck

The time-averaged flow fields described in the previous section result from a complex instantaneous interaction between different flow structures. In order to characterize the velocity fluctuations on the deck, velocity and

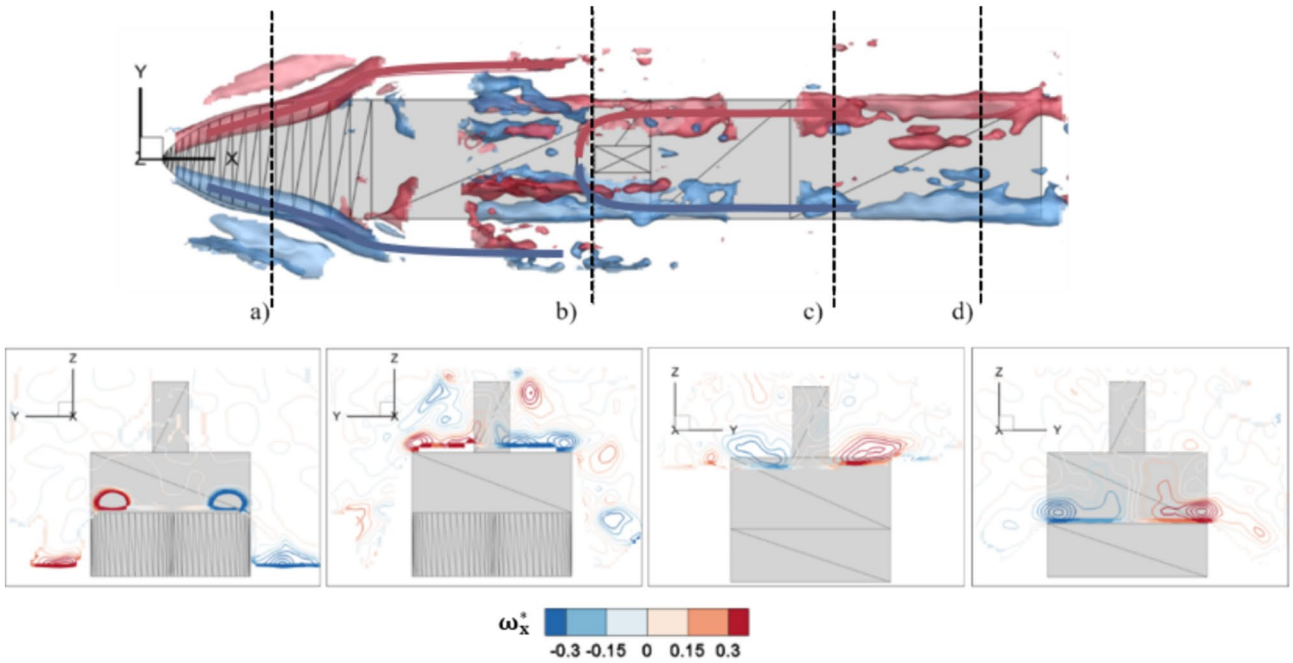


**Fig. 10** Normalized streamwise vorticity iso-surfaces (top) and vertical planes of vorticity contours at specified stations (bottom)

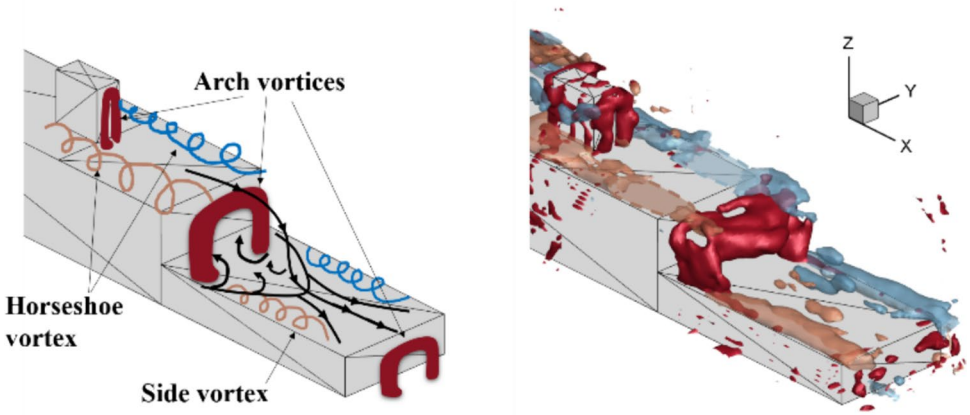


**Fig. 11** (Left) Schematic of the main flow structures expected from the literature studies. (Right) Iso-surfaces of $w^* = -0.25$ and 0.25 and Q-criterion = 0.02 $s.^{-2}$

velocity standard deviation profiles have been extracted at the mid-hangar height $z = H/2$ and mid deck length $x = L/2$, for each component, and are plotted in Fig. 12.

The streamwise velocity component features a symmetrical distribution, with its standard deviation exhibiting a central plateau edged with two mild peaks of approximately 20% intensity, when referred to the free-stream velocity.

Fluctuations in the order of 15% are observed for the vertical and lateral components, which suggests large-scale unsteady behavior of the separated wake.

#### 4.2.1 Modal analysis of unsteady behavior at the rear deck

Further analysis of the wake flow topology is conducted with proper orthogonal decomposition (POD), using the method of snapshots (Sirovich 1987). POD is a mathematical technique to extract the most energetic features of non-homogeneous turbulent flows (Taira et al. 2017). The spatial modes are ranked based on their kinetic energy (KE) levels. The first three modes are the most energetic, collecting approximately 30% of the total energy (Fig. 13). The energy distribution rapidly flattens at the 4th mode, with the first 15

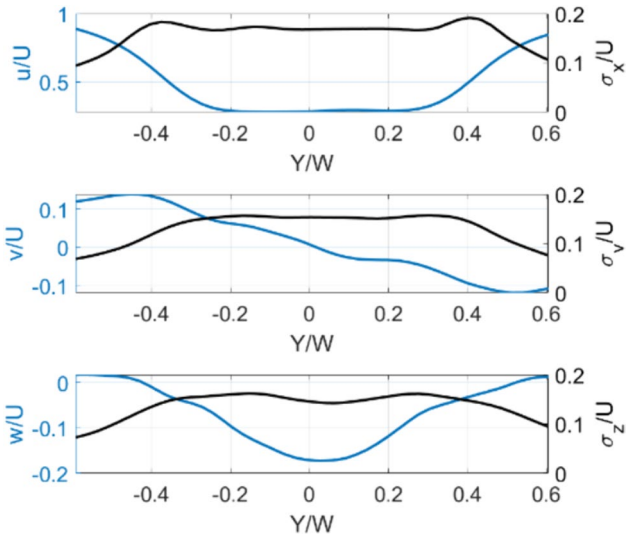


**Fig. 12** Component-wise velocities and standard error on a horizontal plane in the mid-deck: $z = H_B/2$, $x = L/2$

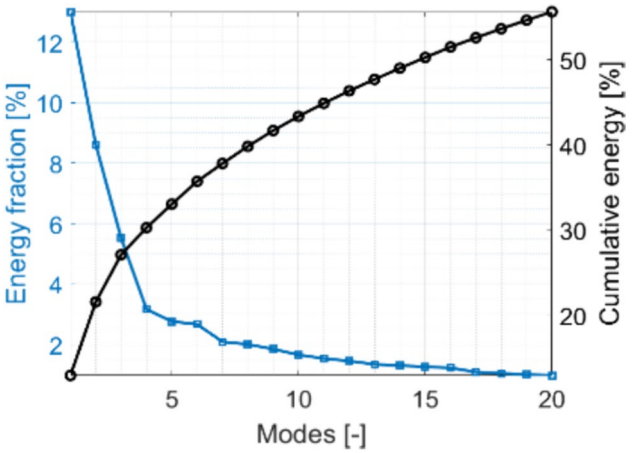


**Fig. 13** Energy distribution in the first 20 POD modes

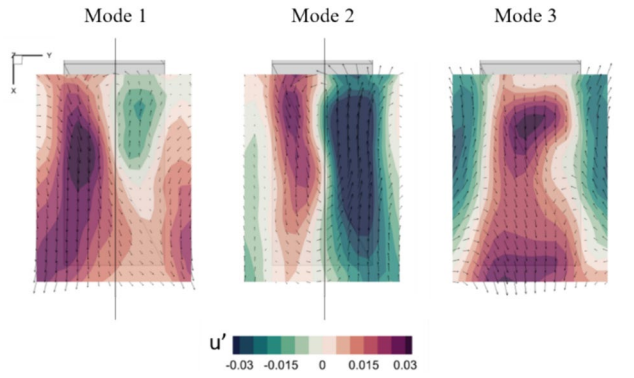


**Fig. 14** Streamwise velocity component of the first three POD modes, on the mid-plane of the flight–deck, $z = H_B/2$

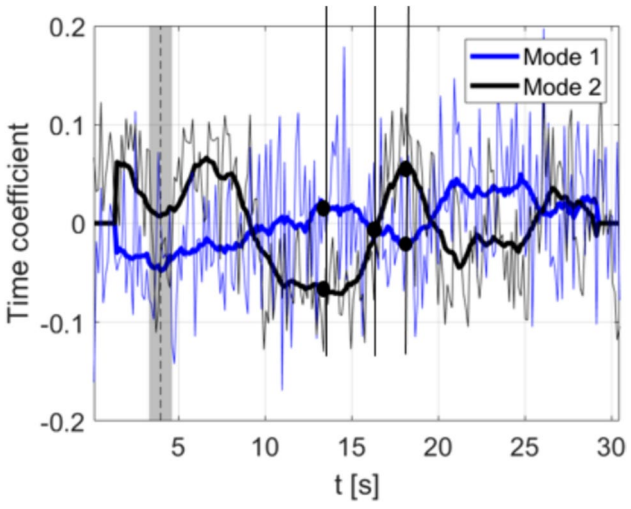


**Fig. 15** Raw and filtered (bold lines) time coefficients of Modes 1 and 2

modes comprising 50% of the total energy. The latter indicates the chaotic nature of the turbulent fluctuations in the separated region, with a broad range of scales contributing to the dynamics of the flow. Here, a short analysis is given for the most energetic modes.

The spatial organization of the first three modes is shown in Fig. 14, by means of streamwise velocity contours selected at the mid-height plane of the flight deck. The first two modes have a similar spatial structure, exhibiting alternating streamwise velocity deficit on the port and starboard sides of the flight deck. The two modes show anti-symmetry along the mid-plane $y = 0$, with one mode more focused on the port side and the other on the starboard side. If considered as a pair, they can capture lateral oscillations of the separated wake flow. Their mirror symmetry suggests that the modes are needed in combination to represent a flow behavior which is inherently symmetric (the geometry is symmetric around the mid-plane and the measurement is done at headwind condition); however, their unequal energy distribution suggests that the flow might be biased toward one side. The two effects combined could be interpreted as evidence that the flow is more aligned with one mode during certain periods and switch during others, while maintaining an overall symmetry in the time-averaged sense. This observation is in line with the previous studies on ship airwakes, that attribute the most energetic flow features to similarly fluctuating, organized flow motion that is bi-stable over the flight–deck.

This is reported in the works of (Herry et al. 2011; Vidales et al. 2016; Mallat and Pastur 2023; Zhu et al. 2024), among others. In order to investigate the possibility of flow bi-stability, the time coefficients of the first two modes were examined, as plotted in Fig. 15.

Bi-stability in this context means that the recirculation region may enter a relatively stable state at either port and starboard side of the flight–deck and only switch position after a long time. In order to define a sufficiently long time period that would suggest stability, a transit time scale is taken to be that taken by a fluid particle to travel across the complete model. In the present experiment, such time is approximately 120 ms. During the observation time of 30 s, at least two cycles of fluctuations are captured, each lasting approximately 15 s. The latter is approximately two orders of magnitude longer than the transit time, supporting the hypothesis of bi-stability of the wake.

Finally, the third mode is associated with a streamwise elongation and contraction of the wake: When the wake elongates in the streamwise direction, it contracts in the lateral direction, thus becoming narrower. Such mode structure represents a dynamic behavior typically reported in 2D BFS studies, as shear layer flapping (Driver et al. 1987).

The present modal analysis is performed on 3D data. However, attention is placed here on the comparison between 3D data decomposition and 2D. Most of the literature has focused onto the vertical plane of symmetry of the deck $y=0$. Figure 16 illustrates the velocity distribution for Mode 1 as obtained from the 2D (left) and 3D (right) analysis. Here, some marked differences are observed in terms of flow topology. Despite these differences, the 2D results compare favorably with the planar PIV experiment by Seth et al. (2021), and what was found by Tinney et al. (2020) in their numerical study.

The first and most energetic mode of the 2D POD analysis shows a streamwise velocity deficit around the reattachment region, and a velocity increases in the first half of the deck, on top of the hangar. This mode describes a dynamic behavior whereby the recirculation region elongates in the streamwise direction and contracts vertically, similar to what is observed in Mode 3 of the 3D decomposition. Additionally from the energy distribution plotted on the right of Fig. 16, it can be seen that in the 2D case, the energy captured in the first mode is approx. 30%, which corresponds to the sum of the first three modes of the 3D decomposition. Therefore, it can be concluded that the 2D POD analysis can mislead the interpretation of the large-scale flow dynamics, in that the presence of the wake's lateral fluctuation (which are the dominant dynamic in 3D) is projected across the measurement plane, but not captured in the lateral motions.

The 3D analysis shows that in fact the wake dynamics are characterized by a lateral flapping of the wake and the change in size of the recirculation bubble behind the superstructure. This is obscured in the 2D POD analysis, highlighting the need for large-scale volumetric flow measurements.

## 5 Conclusion

A large-scale volumetric velocimetry measurement with helium-filled soap bubbles has been performed at the AWT of the NLR with a multi-directional, redundant camera system and multiple illumination directions, to measure the flow field around a ship model at 10 m/s free-stream velocity. The measurement volume attains approximately 0.5 $m^3$, and it is extensively covered using seven cameras and two illumination directions.

The foundational elements of multi-directional redundant illumination and imaging are discussed, with the approaches needed in large-scale 3D-LPT experiments that extend the measurement domain and enable unsteady aerodynamic analysis. An optical loss parameter has been defined as a guideline for volumetric measurements that feature rotations of the model, most specific in the field of wind engineering. Overall, the results showed that a redundant system of cameras operated in a partitioned mode significantly decreases volume coverage losses in the measurement domain and, therefore, allows the study of the global unsteady behavior in multi-directional 3D-LPT systems.

The technique is demonstrated on the relevant problem of ship–wind interaction where velocity measurement was obtained around the ship. Multiple zones with shear

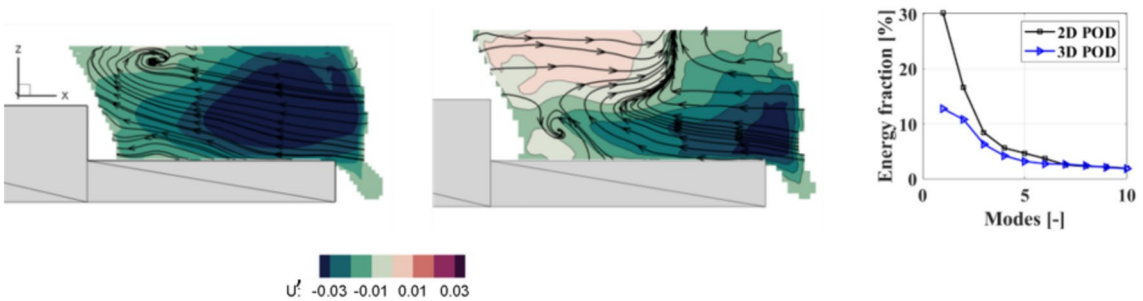


**Fig. 16** Streamlines and contour plots of the streamwise velocity component for: Mode 1 of 2D POD (left) and Mode 3 of 3D POD (middle); plot of the energy distribution in the two decompositions

layers and recirculation regions were observed on both the superstructure and flight–deck. Three-dimensional POD was used to analyze the large-scale unsteady motions on the flight–deck, where the first three modes identify lateral flapping of the wake and the change in size of the recirculation bubble behind the superstructure. The primary modes occur close to the flight deck, at a scale in the order of the deck length, and support previous finding of recirculation region bi-stability.

**Supplementary Information** The online version contains supplementary material available at https://doi.org/10.1007/s00348-024-03867-0.

**Acknowledgements** The help of the wind tunnel technicians Tim Deleij and Laurens de Haan, as well as the technical support of DMO during the project are kindly acknowledged.

**Author contribution** The research concept was initially proposed by M.T. The design of the experimental setup and the measurements were done by I.H, M.T and M.J.M. Data processing was done by I.H. The optical access theoretical considerations and performance parameter definition were done by I.H, F.S, A.S and M.T. I.H drafted the manuscript, which was then critically reviewed by F.S, A.S, M.T, T.R, E.R and M.J.M.

**Funding** This work was performed as a public–private collaboration between NLR and Damen Naval.

**Data availability** No datasets were generated or analyzed during the current study.

## Declarations

**Conflict of interest** The authors declare no competing interests.

**Ethical approval** Not applicable.



## References

Barbosa-Saldaña JG, Anand NK (2007) Flow over a three-dimensional horizontal forward-facing step. Numer Heat Transf Part Appl 53:1–17. https://doi.org/10.1080/10407780701446473

Buchmann NA, Atkinson C, Jeremy MC, Soria J (2011) Tomographic particle image velocimetry investigation of the flow in a modeled human carotid artery bifurcation. Exp Fluids 50:1131. https://doi.org/10.1007/s00348-011-1042-1

Caridi, GAP (2018) Development and application of helium-filled soap bubbles for large-scale PIV experiments in aerodynamics. PhD Thesis, Delft University of Technology. https://doi.org/10.4233/UUID:EFFC65F6-34DF-4EAC-8AD9-3FDB22A294DC

Chovet C, Lippert M, Foucaut J-M, Keirsbulck L (2017) Dynamical aspects of a backward-facing step flow at large Reynolds numbers. Exp Fluids 58:162. https://doi.org/10.1007/s00348-017-2444-5

Chun KB, Sung HJ (1998) Visualization of a locally-forced separated flow over a backward-facing step. Exp Fluids 25:133–142. https://doi.org/10.1007/s003480050217

De Gregorio F, Pengel K, Kindler K (2012) A comprehensive PIV measurement campaign on a fully equipped helicopter model. Exp Fluids 53:37–49. https://doi.org/10.1007/s00348-011-1185-0

Driver DM, Seegmiller HL, Marvin JG (1987) Time-dependent behavior of a reattaching shear layer. AIAA J 25:914–919. https://doi.org/10.2514/3.9722

Eaton JK, Johnston JP (1981) A review of research on subsonic turbulent flow reattachment. AIAA J 19:1093–1100

Elsinga G, Scarano F, Wieneke B, van Oudheusden BW (2006) Tomographic particle image velocimetry. Exp Fluids 41:933–947. https://doi.org/10.1007/s00348-006-0212-z

Elsinga G, Westerweel J, Scarano F, Novara M (2011) On the velocity of ghost particles and the bias error in Tomographic-PIV. Exp Fluids 50:825–838. https://doi.org/10.1007/s00348-010-0930-0

Fahringer TW, Lynch KP, Thurow BS (2015) Volumetric particle image velocimetry with a single plenoptic camera. Meas Sci Technol 26:115201. https://doi.org/10.1088/0957-0233/26/11/115201

Fajardo C, Sick V (2009) Development of a high-speed UV particle image velocimetry technique and application for measurements in internal combustion engines. Exp Fluids 46:43–53. https://doi.org/10.1007/s00348-008-0535-z

Faleiros DE, Tuinstra M, Sciacchitano A, Scarano F (2019) Generation and control of helium-filled soap bubbles for PIV. Exp Fluids 60:40. https://doi.org/10.1007/s00348-019-2687-4

Faleiros, DE (2021) Soap bubbles for large-scale PIV. PhD Thesis, Delft University of Technology. https://doi.org/10.4233/UUID:C579128F-9E96-4E9E-9997-6CE9486E1E25

Graziani A, Kerhervé F, Martinuzzi RJ, Keirsbulck L (2018) Dynamics of the recirculating areas of a forward-facing step. Exp Fluids 59:154. https://doi.org/10.1007/s00348-018-2608-y

Häfeli R, Altheimer M, Butscher D, Rudolf Von Rohr P (2014) PIV study of flow through porous structure using refractive index matching. Exp Fluids 55:1717. https://doi.org/10.1007/s00348-014-1717-5

Healey JV (1992) Establishing a database for flight in the wakes of structures. J Air 29:559–564. https://doi.org/10.2514/3.46202

Herry BB, Keirsbulck L, Labraga L, Paquet J-B (2011) Flow bistability downstream of three-dimensional double backward facing steps at zero-degree sideslip. J Fluids Eng 133:054501. https://doi.org/10.1115/1.4004037

Hoyer K, Holzner M, Lüthi B, Guala M, Liberzon A, Kinzelbach W (2005) 3D scanning particle tracking velocimetry. Exp Fluids 39:923–934. https://doi.org/10.1007/s00348-005-0031-7

Hysa I, Tuinstra M, Sciacchitano A, Scarano F, Schwartz N, Harrison C, Gebbink R (2023) Three-dimensional quantitative flow visualization around a thrust reverser. AIAA J 61:5404–5414

Jahn T, Schanz D, Schröder A (2021) Advanced iterative particle reconstruction for Lagrangian particle tracking. Exp Fluids 62:179

Jux C, Sciacchitano A, Schneiders JFG, Scarano F (2018) Robotic volumetric PIV of a full-scale cyclist. Exp Fluids 59:74

Kulkarni PR, Singh SN, Seshadri V (2005) Flow visualization studies of exhaust smoke-superstructure interaction on naval ships. Nav Eng J 117:41–56

Largeau JF, Moriniere V (2006) Wall pressure fluctuations and topology in separated flows over a forward-facing step. Exp Fluids 42:21–40. https://doi.org/10.1007/s00348-006-0215-9

Maas HG, Gruen A, Papantoniou D (1993) Particle tracking velocimetry in three-dimensional flows: part 1. photogrammetric determination of particle coordinates. Exp Fluids 15:133–146

Maekawa A, Sakakibara J (2018) Development of multiple-eye PIV using mirror array. Meas Sci Technol 29:064011

Mallat B, Pastur LR (2023) Aerodynamics of realistic frigate geometries: conditions for bi-stable wake dynamics. Ocean Eng 277:114311

Miklosovic D, Snyder M, Kang H (2011) Ship air wake wind tunnel test results, 29th AIAA Applied Aerodynamics Conference, Honolulu. Hawaii. https://doi.org/10.2514/6.2011-3155

Muller K, Hemelrijk CK, Westerweel J, Tam DSW (2020) Calibration of multiple cameras for large-scale experiments using a freely moving calibration target. Exp Fluids. https://doi.org/10.1007/s00348-019-2833-z

Piirto M, Saarenrinne P, Eloranta H, Karvinen R (2003) Measuring turbulence energy with PIV in a backward-facing step flow. Exp Fluids 35:219–236

Poelma C (2020) Measurement in opaque flows: a review of measurement techniques for dispersed multiphase flows. Acta Mech 231:2089–2111. https://doi.org/10.1007/s00707-020-02683-x

Raffel M, Bauknecht A, Ramasamy M, Yamauchi GK, Heineck JT, Jenkins LN (2017) Contributions of particle image velocimetry to helicopter aerodynamics. AIAA J 55:2859–2874

Rosenfeld N, Kimmel K, Sydney AJ (2015) Investigation of ship topside modeling practices for wind tunnel experiments, 53rd AIAA aerospace sciences meeting, Kissimmee. Florida. https://doi.org/10.2514/6.2015-0245

Scarano F, Benocci C, Riethmuller ML (1999) Pattern recognition analysis of the turbulent flow past a backward facing step. Phys Fluids 11:3808–3818

Scarano F, Ghaemi S, Caridi GCA, Bosbach J, Dierksheide U, Sciacchitano A (2015) On the use of helium-filled soap bubbles for large-scale tomographic PIV in wind tunnel experiments. Exp Fluids 56:42

Scarano F (2013) Tomographic PIV: principles and practice. Meas Sci Technol 24:012001

Schanz D, Gesemann S, Schröder A (2016) Shake-the-box: lagrangian particle tracking at high particle image densities. Exp Fluids 57:70

Schneiders JFG, Scarano F, Jux C, Sciacchitano A (2018) Coaxial volumetric velocimetry. Meas Sci Technol 29:065201. https://doi.org/10.1088/1361-6501/aab07d

Schröder A, Willert C, Schanz D, Geisler R, Jahn T, Gallas Q, Leclaire B (2020) The flow around a surface mounted cube: a characterization by time-resolved PIV, 3D shake-the-box and LBM simulation. Exp Fluids 61:189

Schröder A, Schanz D (2023) 3D lagrangian particle tracking in fluid mechanics. Annu Rev Fluid Mech 55:511

Sciacchitano A, Giaquinta D, Schneiders JFG, Scarano F, van Rooijen BD, Funes DE (2018) Quantitative flow visualization of a turboprop aircraft by robotic volumetric velocimetry, 18th International Symposium on Flow Visualization. Zurich, Switzerland

Seth D, Leishman JG, Gnanamanickam E, Zhang Z (2021) Time-resolved ship airwake measurements in a simulated atmospheric boundary layer. J Aircr 58:624–649. https://doi.org/10.2514/1.C035886

Sirovich L (1987) Turbulence and the dynamics of coherent structures. I Coherent Struct Q Appl Math 45:561–571. https://doi.org/10.1090/qam/910462

Sousa J (2002) Turbulent flow around a surface-mounted obstacle using 2D–3C DPIV. Exp Fluids 33:854–862. https://doi.org/10.1007/s00348-002-0497-5

Spazzini PG, Iuso G, Onorato M, Zurlo N, Di Cicca GM (2001) Unsteady behavior of back-facing step flow. Exp Fluids 30:551–561. https://doi.org/10.1007/s003480000234

Sung HJ, Lee I, Ahn SK (2004) Three-dimensional coherent structure in a separated and reattaching flow over a backward-facing step. Exp Fluids 36:373–383. https://doi.org/10.1007/s00348-003-0637-6

Taira K, Brunton SL, Dawson STM, Rowley CW, Colonius T, McKeon BJ, Schmidt OT, Gordeyev S, Theofilis V, Ukeiley LS (2017) Modal analysis of fluid flows: an overview. AIAA J 55:4013–4041. https://doi.org/10.2514/1.J056060

Tinney CE, Ukeiley LS (2009) A study of a 3-D double backward-facing step. Exp Fluids 47:427–438. https://doi.org/10.1007/s00348-009-0675-9

Tinney CE, Shipman J, Panickar P (2020) Proper-orthogonal-decomposition-based reduced-order models for characterizing ship airwake interactions. AIAA J 58:633–646. https://doi.org/10.2514/1.J058499

Uzol O, Chow Y-C, Katz J, Meneveau C (2002) Unobstructed particle image velocimetry measurements within an axial turbo-pump using liquid and blades with matched refractive indices. Exp Fluids 33:909–919. https://doi.org/10.1007/s00348-002-0494-8

Van Muijden J, Boelens O, Van Der Vorst J, Gooden J (2013) Computational ship airwake determination to support helicopter-ship dynamic interface assessment, 21st AIAA Computational Fluid Dynamics Conference, San Diego, CA. https://doi.org/10.2514/6.2013-3078

Vidales, AFR (2016) Air-wake flow dynamics on a simplified frigate shape, Master's thesis, Delft University of Technology. https://doi.org/10.13140/RG.2.2.20488.03849

Wall A, Thornhill E, Barber H, McTavish S, Lee R (2022) Experimental investigations into the effect of at-sea conditions on ship airwake characteristics. J Wind Eng Ind Aerodyn 223:104933. https://doi.org/10.1016/j.jweia.2022.104933

Wieneke B (2008) Volume self-calibration for 3D particle image velocimetry. Exp Fluids 45:549–556. https://doi.org/10.1007/s00348-008-0521-5

Wieneke B (2013) Iterative reconstruction of volumetric particle distribution. Meas Sci Technol 24:024008. https://doi.org/10.1088/0957-0233/24/2/024008

Zan S (2005) On aerodynamic modelling and simulation of the dynamic interface. J Aerosp Eng 219:393–410

Zhu N, Zhang Z, Gnanamanickam EP, Leishman JG (2024) Estimation of 3D ship airwakes using dual-plane PIV. Exp Fluids 65:11. https://doi.org/10.1007/s00348-023-03727-3